Magnetoelectric Backscatter Communication for Millimeter-Sized Wireless Biomedical Implants

Zhanghao Yu*, Fatima T. Alrashdan*, Wei Wang, Matthew Parker, Xinyu Chen†, Frank Y. Chen§, Joshua Woods, Zhiyu Chen, Jacob T. Robinson#, Kaiyuan Yang#
Rice University, Houston, TX, USA

ABSTRACT

This paper presents the design, implementation, and experimental evaluation of a wireless biomedical implant platform exploiting the magnetoelectric effect for wireless power and bi-directional communication. As an emerging wireless power transfer method, magnetoelectric is promising for mm-scaled bio-implants because of its superior misalignment sensitivity, high efficiency, and low tissue absorption compared to other modalities [46, 59, 60]. Utilizing the same physical mechanism for power and communication is critical for implant miniaturization, but low-power magnetoelectric uplink communication has not been achieved yet. For the first time, we design and demonstrate near-zero power magnetoelectric backscatter from the mm-sized implants by exploiting the converse magnetostriction effects.

The system for demonstration consists of an 8.2-mm^3 wireless implantable device and a custom portable transceiver. The implant's ASIC interfacing with the magnetoelectric transducer encodes uplink data by changing the transducer's load, resulting in resonance frequency changes for frequency-shift-keying modulation. The magnetoelectrically backscattered signal is sensed and demodulated through frequency-to-digital conversion by the external transceiver. With design optimizations in data modulation and recovery, the proposed system archives > 1-kbps data rate at the 335-kHz carrier frequency, with a communication distance greater than 2 cm and a bit error rate less than 1E-3. Further, we validate the proposed system for wireless stimulation and sensing, and conducted ex-vivo tests through a 1.5-cm porcine tissue. The proposed magnetoelectric backscatter approach provides a path towards miniaturized wireless bio-implants for advanced biomedical applications like closed-loop neuromodulation.

CCS CONCEPTS

• **Hardware → Wireless devices**; *Neural systems.*

KEYWORDS

Magnetoelectric, backscatter communication, wireless biomedical implants, bioelectronics

ACM Reference Format:
Zhanghao Yu*, Fatima T. Alrashdan*, Wei Wang, Matthew Parker, Xinyu Chen†, Frank Y. Chen§, Joshua Woods, Zhiyu Chen, Jacob T. Robinson#, Kaiyuan Yang#. 2022. Magnetoelectric Backscatter Communication for Millimeter-Sized Wireless Biomedical Implants. In *The 28th Annual International Conference On Mobile Computing And Networking (ACM MobiCom '22), October 17–21, 2022, Sydney, NSW, Australia.* ACM, New York, NY, USA, 14 pages. https://doi.org/10.1145/3495243.3560541

1 INTRODUCTION

Wireless implantable bioelectronics promise revolutionary clinical therapies, such as treating neurological and psychiatric disorders by interfering directly with the nervous system [4, 6, 13, 14, 21, 23, 29, 31, 34, 38–40, 42, 45, 57, 59, 60]. These devices deliver controlled stimulation to modulate the electrical activities of the nervous system [6, 13, 23, 38–40, 59, 60] and/or record electrical, chemical, and physical properties for better diagnosis [4, 14, 21, 29, 31, 34, 42, 57].

The crucial challenge in the design of wireless bio-implants is to reliably power and communicate with miniaturized implants. While batteries have been the conventional power source of medical implants for a long time, the last decade has seen a transition to wireless power transfer solutions that feature smaller footprints, less weight, longer lifetime, and less invasive implantation procedures [23, 40, 42]. Various wireless power transfer technologies including radio frequency (RF) [1, 30, 31, 38], inductive coupling [4, 13, 21, 23, 33, 57], ultrasound [14, 39, 42, 43, 48], and light [29, 34] have demonstrated the ability to wireless power medical implants. However, they face trade-offs and limitations among at least one of the following properties: receiver size, misalignment tolerance, transmission loss, and power that can safely be delivered through the biological tissues.

Magnetoelectric (ME) is an emerging technology for wirelessly powering mm-sized devices deep inside the body, by converting low-frequency (hundreds of kHz) magnetic fields to electric voltage through ME transducers [3, 6, 17, 41, 45, 46, 53, 59–61]. It owns several critical advantages including high efficiency with miniaturized size, high power delivery (> 1 mW) without safety issues, and high misalignment tolerance [3, 6, 17, 59, 60]. These features are empowered by using ME materials that have high power density, low mechanical resonance frequency, and high permeability to concentrate magnetic flux inside the material [11, 45, 59, 60].

Integrating the ME thin-film transducer with an application-specific integrated circuit (ASIC) chip forms the ME implant that enables both wireless power transfer and data downlink through

* These authors contributed equally to this paper.
† This author is now at the University of Michigan, Ann Arbor.
§ This author is now at SambaNova Systems.
# Corresponding Authors (Email: {jtrobinson, kyang}@rice.edu).

ACM MobiCom '22, October 17–21, 2022, Sydney, NSW, Australia

ACM ISBN 978-1-4503-9181-8/22/10…$15.00
https://doi.org/10.1145/3495243.3560541

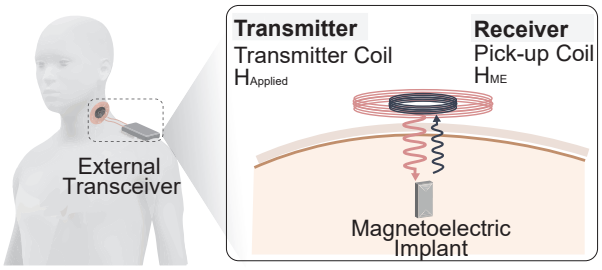

Figure 1: Overview of the proposed magnetoelectric wireless bio-implant platform. It achieves wireless power and bidirectional communication using a single magnetoelectric transducer.

modulation of the magnetic field from an external ME transmitter to the implant to digitally program the stimulation parameters [6, 59–61]. However, compared to other wireless technologies like RF, inductive coupling, and ultrasound, there have been no demonstrations of using ME backscatter to efficiently send data from the implant to the external transceiver (TRX). Uplink communications are useful for bio-implants to report sensor data for closed-loop applications and to monitor and calibrate device operation conditions. Although integrating the ME implants with another communication module, like RF antennas, inductive coils, piezoelectric transducers, or LEDs, is an engineering workaround [61], sharing the same mechanism for wireless power and communication can greatly facilitate device miniaturization and improve system efficiency.

To tackle this issue, we propose a novel ME backscatter technology for uplink communication, by leveraging the converse magnetostriction effects [8, 54]. We further demonstrate the first mm-sized batteryless biomedical implant platform exploiting ME effects for both wireless powering and bi-directional communication (see Figure 1). Our key finding is modulating the electric load of the ME transducer leads to the ME resonance frequency change for frequency-shift-keying (FSK) modulation. In this work, capacitive load shift is implemented in the implant's ASIC to maximize the resonance frequency change without substantial fluctuations of received voltage. The system consists of an external custom transceiver (TRX) and an implant integrating a 1×1.5-mm^2 ASIC chip, a 2×5×0.28-mm^3 ME transducer, a 0.25-mm^3, 22-μF energy storage capacitor, and 1-mm^2 onboard electrodes within an 8.2-mm^3 volume (see Figure 2).

As shown in Figure 3, the implant wirelessly receives power to generate proper power supplies, communicates with the TRX, senses the received voltage and the ambient temperature, and delivers programmable electrical stimulus. The custom ME TRX includes a power transmitter (TX), a backscatter receiver (RX), and a controller. The power TX connects a coil to apply the 335-kHz excitation magnetic field to deliver power and downlink data. The backscatter RX equips a pick-up coil to sense the backscattered magnetic field generated by the implant and demodulate uplink data. The controller synchronizes the TX and the RX and remotely programs the implant's operation by controlling the generation of the applied magnetic field.

The proposed system achieves a maximum data rate of 8 kbps in uplink with a 335-kHz frequency of the excitation magnetic field. The performance of ME backscatter is experimentally assessed

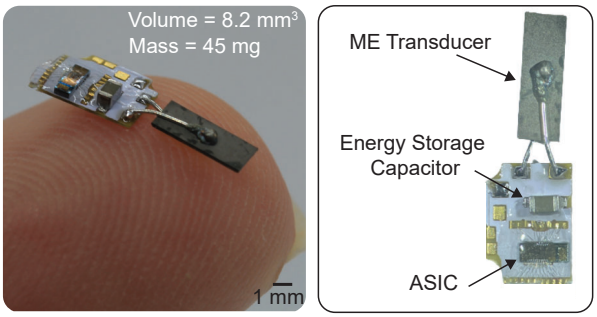

Figure 2: The prototyped magnetoelectric (ME) implant. The implant is shown on a fingertip to illustrate its miniaturized form factor. It integrates an ASIC chip, a ME transducer, and an energy storage capacitor onto the board with an 8.2-mm^3 volume and a 45-mg weight.

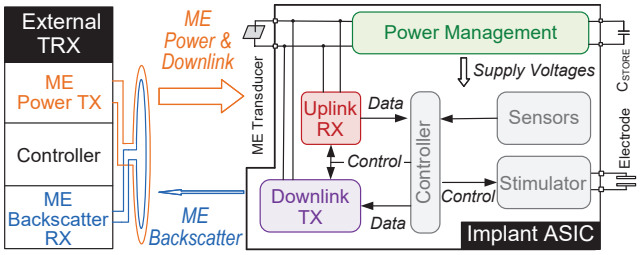

Figure 3: System diagram. The proposed wireless system consists of a custom transceiver and an mm-sized implant. The power and downlink data are wirelessly delivered through the ME effect; the ME backscatter is exploited for uplink communication.

by measuring the signal-to-noise ratio (SNR) and bit-error rate (BER) at various TRX-implant distances. Furthermore, techniques to improve the ME backscatter's robustness and communication range are discussed and evaluated. With the design optimizations, the prototype system achieves a BER less than 1E-3 at a 2-cm distance. Finally, we validated the proposed system's performance *ex vivo* with a 1.5-cm thick porcine tissue.

2 BACKGROUND

2.1 Wireless Power and Communication Technologies for Miniature Implants

While significant advancement has been made in developing wireless techniques for miniature biomedical implants, there remain critical limitations to existing approaches. RF electromagnetic (EM) is capable of powering and communicating the implanted devices in far field [1, 31, 38]. However, it wrestles with the antenna size constraint requiring the dimension to be comparable to the EM wavelength. The mm-scale implants usually require > Ghz carrier frequencies [1, 26, 30, 31], raising concerns about body absorption. Inductive coupling has been widely used in wireless implantable system because of its flexible capability for charging and bi-directional telemetry [22, 51, 57]. However, the coupling is sensitive to the variations in distance and direction, especially when the implant coil is small [4, 12, 24]. Additionally, most inductively powered devices work at 13.56 MHz or higher frequencies for better efficiency [2, 21, 30, 51], resulting in substantial energy absorbed by the

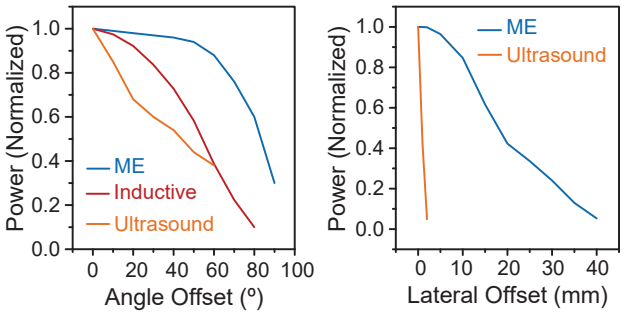

Figure 4: Misalignment sensitivity of different wireless power transfer techniques. Implants' received power decreases with angle and lateral offset. Measured misalignment tolerance of ME power transfer is superior to inductive coupling [4] and ultrasound [39].

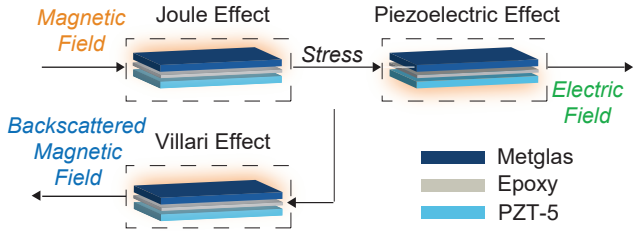

Figure 5: Illustration of the ME effects. Magnetoelectric composites combine magnetostrictive material (Metglas) and piezoelectric material (PZT-5) to convert magnetic energy to electric energy and vice versa. The direct magnetostriction effect (Joule effect) converts the applied magnetic field into mechanical stress. At the same time, the generated stress changes the material magnetization in the form of a backscattered magnetic field according to the converse magnetostriction effect (Villari effect). The PZT-5 turns the mechanical stress into an electric voltage across the composite.

body and requiring operation under certain restrictions [47]. While ultrasound [14, 39, 42, 43, 48] and optics [29, 34] have shown promising potentials in wirelessly transmitting power and data, they suffer from energy loss due to reflection or scattering when transferring through different tissue layers, limiting their efficiency [7, 16].

Recently proposed ME power transfer is a promising technology to circumvent these challenges [3, 6, 17, 41, 45, 46, 52, 59–61], especially for powering millimeter-sized implants [6, 45, 59–61]. First, the ME transducer's voltage coefficient is almost independent of the transducer's width and length [59, 63]. As a result, the ME effects have great potential to maintain good efficiency with miniaturization [60]. For example, the ME implant recently reported by [61] achieves a power transfer efficiency that is 4× higher than [39, 51] and 10× higher than [30]. All these implants are millimeter-scale, while [39] is ultrasonically powered and [30, 51] adopt inductive-coupling power transfer. In addition, thanks to the high permeability, the magnetostrictive materials significantly concentrate magnetic flux [11], remarkably boosting the ME power transfer's robustness to misalignment [6, 59, 60]. As shown in Figure 4, compared to the state-of-the-art inductive coupling [4], the ME implants are more tolerant to angular misalignment in power reception. ME is also less sensitive to angles and lateral offsets than ultrasound-based wireless transfers that require focused sound waves [39]. Finally, the sub-MHz low resonance frequency of ME leads to lower tissue absorption, and a stronger magnetic field is allowed without violating safety limits [59]. It results in order-of-magnitude higher power that can be safely delivered to the implants deep inside the body compared to high-frequency inductive coupling or RF [2, 60]. Specifically, a ME implant working at the 335-kHz resonance frequency is able to receive a peak power of 3.8 mW at 3 cm under EM exposure limits, which is 0.4 mW for the 13.56-MHz inductive coupling counterpart [2, 18].

However, despite a number of recent system demonstrating ME power and downlink data transfer to millimetric implants [6, 45, 59–61], there has been no successful demonstrations of using the ME effects to efficiently transfer uplink data from the implant to the external TRX. While exiting communication methods like inductive coupling backscatter can be integrated into magnetoelectrically powered implants [61], it undoubtedly complicates device integration and prevents further miniaturization of the implants, compared to the potential of achieving powering and bi-directional communication with a single ME transducer. A magnetoelectric antenna reported in [9] demonstrated ME material's capability of communication. Although it achieves a 0.1-kbps data rate at distances longer than 1 m by generating a radiation field, it requires a large size of 10 cm^2, a high excitation voltage of 80 V, and high power consumption of 400 mW, preventing it from being used in wireless miniature implants.

2.2 Backscatter Communication in Implantable Devices

Due to the implant's severely restricted size and power budget, transmitting data from the implants to the external transceiver has long been a challenge. To take advantage of the highly asymmetric energy budget between a battery-free implant and an external transceiver, passive backscatter communication that employs the physical principle of reflecting waves is widely exploited for bioelectronic implants [1, 10, 20, 30, 30, 33, 36, 37, 37, 48, 51, 51, 57, 57]. Compared to active radio broadcasting, the passive backscatter neither generates carrier signals nor amplifies transmission signals, eliminating energy-starved radio circuits such as power amplifiers to make its power overhead negligible [1, 20, 35, 37]. More importantly, a number of wireless battery-free bio-implants have successfully utilized the same physical mechanism for wireless power and backscatter uplink communication across the distance of a few millimeters to a few centimeters, based on electromagnetics [1, 10, 30, 36], inductively coupling [33, 37, 51, 57], and ultrasound waves [14, 42, 43, 48]. The low-power backscatter communication empowered the implantable system to wirelessly record neural signals [14, 30, 42, 57], monitor deep-tissue temperature or oxygenation [43, 48], and regulate system operations [1, 33].

3 MAGNETOELECTRIC BACKSCATTER

3.1 Principle and Physical Model

Our magnetoelectric (ME) transducers are fabricated using a bilayer sheet consisting of a magnetostrictive layer and a piezoelectric layer. The magnetostrictive layer uses 27-μm Metglas (Metglas. Inc), and the piezoelectric layer uses 254-μm-thick lead zirconium titanate

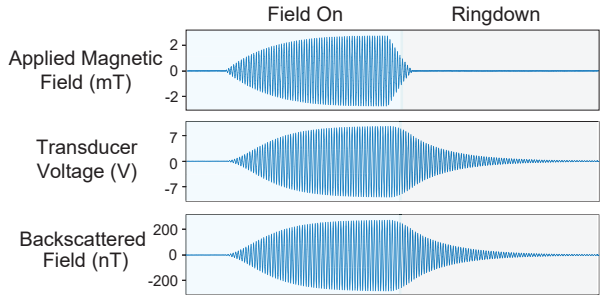

Figure 6: ME transducer's behavior during the field-on and ringdown periods. When the magnetic field is on, the ME transducer vibrates at the excitation field's frequency and generate an electric voltage in addition to the backscattered field. During the ring-down period, the ME transducer will dissipate the stored mechanical energy in form of vibrations at its mechanical resonance frequency, hence the voltage, as well as the backscattered field, will oscillate at the same resonance frequency.

PZT-5 (Piezo. Inc) material. We attached the two layers using M-bond epoxy resin (VPG.Inc), and laser cut the sheet into 5x2 mm^2 films.

When an external magnetic field is applied, mechanical vibrations are generated in the magnetostrictive layer due to the Joule effect shown in Figure 5. Since the magnetostrictive layer and the piezoelectric layer are mechanically coupled, these vibrations are transferred to the piezoelectric layer to create an electric potential across the transducer due to the direct piezoelectric effect. This effect has been leveraged to wirelessly transfer power and downlink data to bio-implants from an external TRX through an alternating magnetic field [3, 6, 59, 60].

The vibrations generated in the magnetostrictive layer will result in a change in the material magnetization, because of the Villari effect [8, 54]. This change can be seen as a backscattered field generated by the ME transducer. Hence, we thought that utilizing these echoes as backscattered signals would enable uplink data transfer from the ME implant to an external TRX. However, during the on-time of the applied field, the ME materials vibrate at the applied field frequency. In this case, the generated backscattered field oscillates at the same excitation frequency, making it challenging to decouple these two signals. To isolate the transducer's response, we measured the backscattered field during the ring-down period when the excitation field is off, as shown in Figure 6. Over the ring-down period, the ME transducer dissipates the stored mechanical energy in the form of decaying voltage at its mechanical resonance frequency irrespective of the excitation field frequency.

3.2 Modulation Mechanism

To modulate the backscattered signal for transmitting data, we need means to change the backscattered field's characteristics at the implant side. Although the field is generated by the magnetostrictive layer, modulating the characteristics of either the piezoelectric layer, magnetostrictive layer, or both will affect the backscattered field due to the mechanical coupling. The modulation of the field can be done by controlling the effective mechanical, magnetic, or electric properties of the composite. For wireless sensing applications,

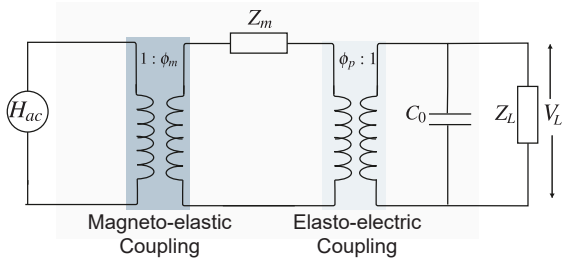

Figure 7: Equivalent circuit model of the ME transducer connected to an electric load.

magnetostrictive materials can be coated with a thin layer of stimuli-responsive polymers that respond to external stimuli by shifting the overall mass hence mechanically modulating the resonance frequency of the sensor [15]. However, the requirements of specific stimuli of magnetism, temperature, strain, or chemical signal limit their compatibility with common electronic circuits. On the other hand, modulating the electric loading conditions has been adopted to tune the resonance frequency of the piezoelectric resonators by changing the electric damping [64]. For our communication system, we utilize the electric loading modulation technique to tune the characteristics of the backscattered field. This specific choice is because it is easier to control this condition inside the body with a simple electronic circuit connected directly to the ME transducer. The electric load can be either active load: DC biasing voltage [49] or passive load: inductive, resistive, capacitive, or a combination of them. We used the passive loads to maintain the miniaturized footprint of the device and avoid any constraints on the power budget. Inductive loads are capable of changing both the mechanical and electrical resonance characteristics of the transducer, however, inductor may cause EMI problems and is usually bulky, hence, we decided to implement either capacitive or resistive load.

3.3 Load Effect Analysis

We used the equivalent circuit model shown in Figure 7 to study the effect of such loads on the ME transducer characteristics. We updated the model given in [3, 53] to account for different loading conditions. Both the voltage across the transducer and the backscattered field result from the mechanical vibrations in the Metglas layer; hence a change in the output voltage's amplitude and frequency implies a change in the amplitude and frequency of the backscattered field. The voltage across the ME transducer connected in parallel to a resistive load R_L :

$$V_L(\omega, R_L) = \frac{\phi_m \phi_p R_L}{R_L(\phi_p^2 + j\omega C_0) + Z_m} H$$

Whereas the voltage across the transducer connected in parallel to a capacitive load C_L:

$$V_L(\omega, C_L) = \frac{\phi_m \phi_p}{\phi_p^2 + j\omega Z_m (C_0 + C_L)} H$$

Where $\phi_m = W t_m \frac{d_{m,33}}{s_m}$ and $\phi_p = W \frac{d_{p,31}}{s_p}$ are the magneto-elastic and electro-elastic coupling factors, $C_0 = \frac{LW\epsilon_p}{t_p}$ is the clamping capacitance of the PZT-5 laminate, and $Z_m = Rm + j\omega L_m + 1/(j\omega C_m)$ represents the mechanical impedance, where $R_m = \frac{\pi v A \rho}{8Q}$, $L_m =$

Table 1: Material properties of Metglas and PZT-5 laminates and equivalent circuit model parameters.

	PZT-5	Metglas
Material Density ρ_p, ρ_m (kg/m^3)	7800	7180
Elastic Compliance s_p, s_m (m^2/N)	19.2×10^{-12}	9.09×10^{-12}
Piezoelectric/Piezomagnetic Coefficient $d_{p,31}$, $d_{m,33}$ $(m/V, Wb/N)$	-190×10^{-12}	8.25×10^{-9}
Relative Permittivity ϵ_p, μ_m	1800	45000
Thickness t_p, t_m (μm)	254	26
Length $L \times$ Width W (mm)	5×2	

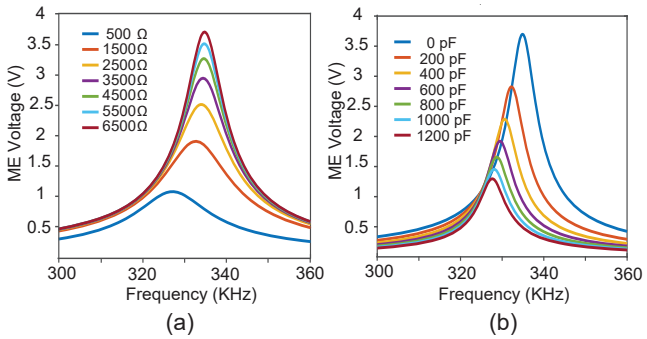

Figure 8: ME transducer's output voltage for different resistive and capacitive loads. Calculated ME voltage waveform using the equivalent circuit model as a function of the applied field frequency for different (a) resistive loads and (b) capacitive loads. Both the resonance frequency and peak voltage are functions of the connected load.

$\frac{\pi v A \rho}{8\omega_r}$, $C_m = \frac{8}{\pi v A \rho \omega_r}$, and Q is the mechanical quality factor. The cross-sectional area of the laminate is defined as $A = A_1 + A_2$ where A_1, A_2 represents the cross-sectional area of the PZT-5 and Metglas laminates respectively, the geometric ratio $n = \frac{A_1}{A_1+A_2} = \frac{t_p}{t_p+t_m}$, the average density $\overline{\rho} = \frac{\rho_p+(\rho_m A_2/k)}{A_1+A_2}$ and the sound velocity $v^2 = \frac{1}{\overline{\rho}}(\frac{n}{s_p} + \frac{1-n}{k s_m})$. The applied AC magnetic field has an amplitude H and frequency ω. The material properties as well as the geometrical parameters are defined in Table 1.

As shown in Figure 8, changing the capacitive or resistive loads across the ME transducer changes the voltage across the transducer as well as its resonance frequency. Consequently, the backscattered field's amplitude and frequency during the ringdown period are changed. The frequency shift is more immune to the depth variation and misalignment that are often unavoidable when the device is implanted; therefore, we used frequency modulation to encode the uplink data.

3.4 Implementation

We adopt the capacitive load-shift-keying (LSK) modulation because it results in a larger frequency shift and smaller voltage drop to help resolve the frequency difference at the TRX circuit and improve the SNR. According to the results shown in Figure 8, shifting the capacitive load from 0 to 200 pF results in a greater-than-3-kHz change in the resonance frequency with a merely 23% drop in the voltage, whereas shifting the resistive load from 5800 Ω to 4800 Ω leads to the same voltage drop but a less than 1 kHz frequency shift. To ensure the robustness and simplicity of the circuit, we use the LSK-induced frequency-shift keying (FSK) to digitally encode the data by switching between two load conditions: an open circuit and a capacitive load. To determine the suitable capacitive load to be implemented on the ASIC chip, we measured the resonance frequency of the ME transducer while connected in parallel to different capacitive loads and compared that with the mathematical model for validation (see Figure 9). The curve of resonance frequency versus capacitive load has the maximum slope when the transducer's load is approximately 100 pF.

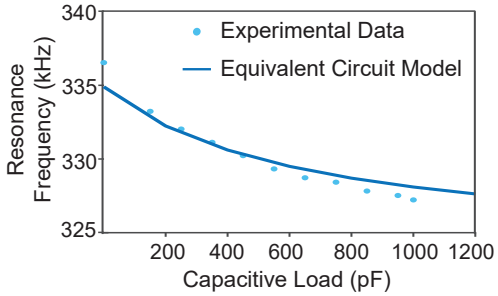

Figure 9: The resonance frequency of the ME transducer for different capacitive loads.

4 IMPLANT ASIC DESIGN

4.1 Overview

The ASIC incorporates a variety of functions including power management, bi-directional communication, sensing, and neural stimulation with 10-μW power consumption, as shown in Figure 10.

4.1.1 Power Management. The power management module interfaces with a ME transducer for energy harvesting and generates proper supply voltages for the entire chip. AC voltage induced on the ME transducer is rectified to a DC voltage V_{RECT} by a active rectifier [25]. Then V_{RECT} is regulated by a switched-capacitor DC-DC power converter to provide supply voltage for the voltage reference generator and the low-dropout regulator (LDO). The DC-DC converter also charges the off-chip capacitor to V_{STIM} to buffer energy for high-power stimulation [60]. A 1-V constant supply V_{STIM} is generated by the LDO for the low-power digital circuitry.

4.1.2 Downlink Telemetry. The implant receives the downlink data simultaneously with the ME power. Simultaneous power and data transfers are usually constrained by the tradeoff between the antenna/transducer's efficiency and bandwidth. To address this challenge, the downlink data is modulated by a time-domain scheme, in which multiple bits are encoded into the duration of a single pulse to amortize the transducer's low switching speed [61]. The data from the TRX is recovered by the ASIC through a time-to-digital converter to program its operation and stimulation parameters. The clock recovery circuit extracts a process- and voltage-invariant timing reference from the ME source and provides clock signals at proper frequencies for the entire system.

4.1.3 Sensing. The ASIC senses implant-received voltage for operation regulation and temperature for in-body thermal monitoring.

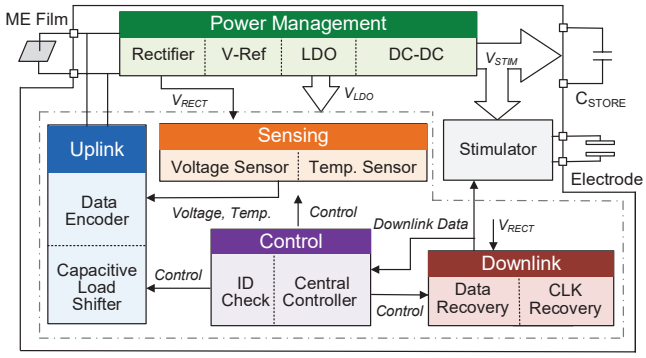

Figure 10: Implant ASIC diagram. The ASIC performs power recovery, communication, voltage and temperature sensing, and neurostimulation.

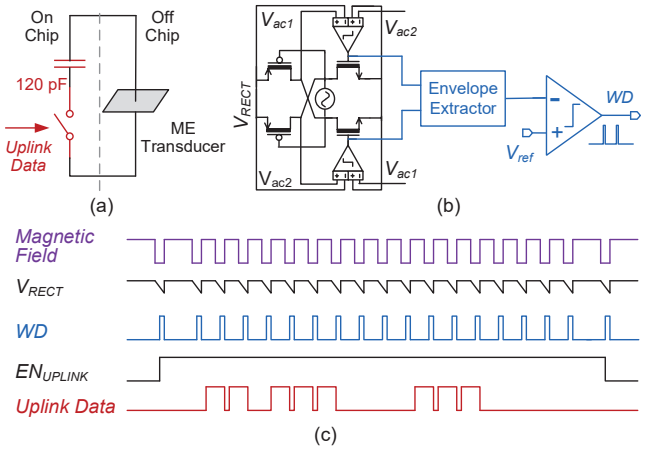

Figure 11: ASIC uplink communication circuit implementation. (a) Schematic of capacitive LSK modulation for changing the ME transducer's resonance frequency; (b) schematic of the magnetic field notch detection circuit; and (c) a timing diagram showing the synchronization with the external TRX.

The voltage sensing is performed by an 8-bit analog-to-digital converter whose core is a voltage-controlled oscillator (VCO). The VCO's output frequency lineally changes with the implant input voltage. The 16-bit temperature sensor is implemented by a low-power ring-oscillator with a native transistor for local voltage regulation [56]. It leverages subthreshold oscillation dependence for temperature monitoring with merely 10-nW power consumption.

4.1.4 Uplink Telemetry. The ASIC's uplink module is designed to transmit the voltage and temperature sensor data to the external TRX through the ME backscatter. The circuit modulates the capacitive load on the ME transducer to shift the frequency of the backscattered signal. The uplink module does not include any active-radio components, so its power consumption is negligible (< 5 nW).

4.1.5 Stimulation. The voltage-controlled stimulation pulses are generated by the stimulation driver and delivered through the electrodes to the target tissue. They own fully programmable parameters, including amplitude (0.5 to 2.5 V, 4 bits), shape (bi-phasic or mono-phasic), pulse width (0.05 to 1.5 ms, 3 bits), and frequency (0 to 200 Hz). Thanks to the adaptive power conversion strategy, the stimulation generation maintains a > 90% efficiency when the amplitude is higher than 1.5 V [60].

4.2 Capacitive Load-Shift-Keying for Backscatter Communication

As discussed in Section 3, to simultaneously achieve large frequency change, high power transfer efficiency, and simple implementation, the implant ASIC uses capacitive LSK to modulate the ME transducer's resonance. The load capacitor is built on chip, as shown in Figure 11 (a). In spite of the fact that a larger capacitor can result in a greater resonance frequency change, it will cause a greater voltage reduction in the ME transducer, reducing the amplitude of backscattered signals. Moreover, a larger capacitor consumes more silicon area. These trade-offs lead us to use a 120-pF capacitor, which produces a frequency change of 3 kHz and a voltage drop of less than 0.5 volts. The on-chip capacitor utilizes both metal-insulator-metal and metal-oxide-metal layers to achieve a density of 2.2 fF/μm^2 and only occupies a area of 0.054 mm^2. When transmitting bit "1", the ASIC connects the 120-pF load to the ME transducer to change the resonance frequency by approximately 3 kHz. The 3-kHz frequency change leads to a 27-ns difference in one period of the backscattered signal. Theoretically, it can be detected by a reference clock higher than 100 MHz, which is available in most micro-controllers. Including multiple periods of backscattered signal can expand the time difference for more accurate detection of resonance frequency change, which will be explained in further details in Section 5.

4.3 Synchronization with the External Transceiver

Since ME backscattered fields can only be detected when the applied magnetic field is off, the implant's ASIC must be synchronized with the external TRX. To ensure that, we designed a scheme that detects the absence of the magnetic field to control the ASIC's operation phases. The magnetic filed will be turned off in a short time (around 90 μs) to generate a narrow notch, which can be quickly detected by the active rectifier's comparator (see Figure 11 (b)) [60]. In the magnetic field notches, the active rectifier's comparator stops generating output pulses that enable load charging. Thus, the envelope of the comparator output is extracted and digitized to a watchdog signal WD to indicate the magnetic field's absence.

Figure 11 (c) illustrates the timing diagram when the implant transmits the 16-bit temperature sensing result to the external TRX. The notch detection circuit monitors the voltage across the ME transducer and generates a pulse (WD) when there is no magnetic field present. Two WD pulses are used to generate a control signal (EN_{UPLINK}) to enable uplink communication. When EN_{UPLINK} becomes high, the following WD pulses will be used for controlling every single bit's transmission. The load is connected to the transducer before the turnoff, ensuring the new frequency settles down at the moment that the TRX starts process the backscattered signal. With this mechanism, the implant's operation is synchronized with the external TRX in a flexible manner.

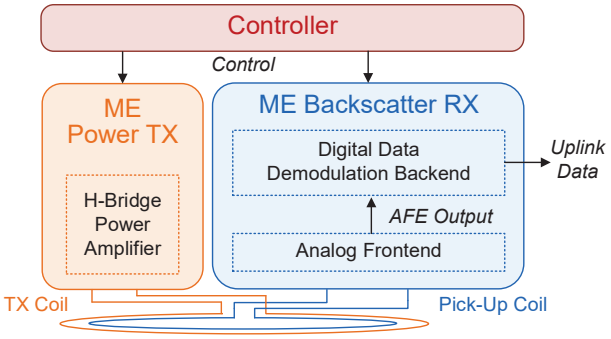

Figure 12: External transceiver overview. The external TRX consists of a ME power TX, a ME backscatter RX and a controller. It equips a TX coil for power and downlink data transfers and a pick-up coil for backscatter sensing.

5 CUSTOM TRANSCEIVER (TRX) DESIGN

5.1 Overview

The external TRX includes a power TX, a backscatter RX, a controller, a 7-cm planar TX coil, and a 2-cm planar pick-up coil to power and communicate with the implant, as shown in Figure 12. A power amplifier based on an H-bridge injects AC current into the TX coil to produce a magnetic field of 335 kHz. In the backscatter RX, an analog frontend (AFE) amplifies the ME backscattered signal in the pick-up coil and generates recovered pulses for the digital backend for data demodulation. The TRX's controller is in charge of the operations of the entire system. To power the implant, it turns on the power amplifier to apply the alternating magnetic field. By disabling the power amplifier in a short time, it generates magnetic field notches to switch the implant's functions such as communication, sensing, and stimulation. Using this strategy, all the components in the system are synchronized.

In the demonstration system, the power amplifier and the AFE are built with commercial electronic components soldered on printed circuit boards. The data demodulation backend circuit and the control module are implemented by the field programmable gate arrays (FPGA). The overall power consumed by the TRX is dominated by the power for wireless power transfer, which varies with channel efficiency. To deliver 2-mW input power to a ME implant at 3 cm in air, the TX consumes 4.5-W power.

5.2 Backscatter Receiver Design

5.2.1 Analog Frontend Design. The AFE for amplification and digitization is built with a analog multiplexer (MUX), a active low-pass filter (LPF), a low-noise instrumentation amplifier, and a high-speed comparator (see Figure 13 (a)). The pick-up coil's voltage can be very high in the power transfer phase due to strong inductive coupling to the TX coil. Thus, the AFE uses a MUX with high-voltage tolerance in the input stage to block the input voltage when the applied magnetic field is on. The MUX is turned on by EN_{LISTEN} during the uplink data transmission to pass the backscattered signal $V_{\text{RX\_COIL}}$ sensed by the pick-up coil, as illustrated in Figure 13 (b). High-frequency noise and interference can be filtered out by the LPF featuring a 375-kHz bandwidth, whose output is amplified by the instrumentation amplifier with a gain of 60 dB. Finally, the comparator converts the amplifier's output to a train of digital pulses,

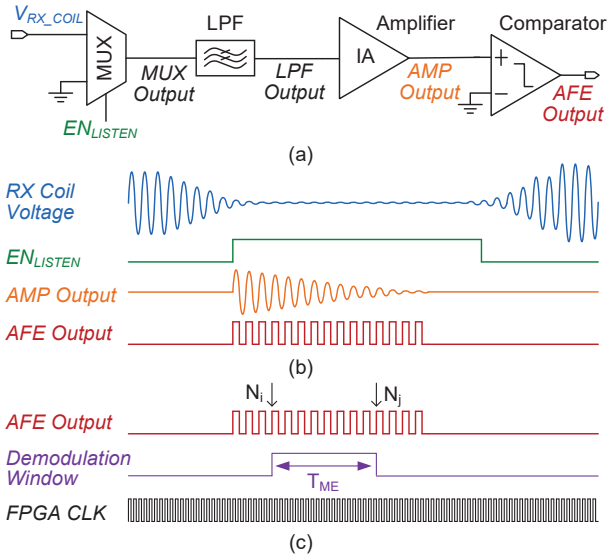

Figure 13: Backscatter RX implementation. (a) Schematic of the analog frontend for the backscattered signal's amplification and digitization; (b) operating waveform diagram of the AFE circuit; and (c) operating waveform diagram of the digital demodulation backend circuit.

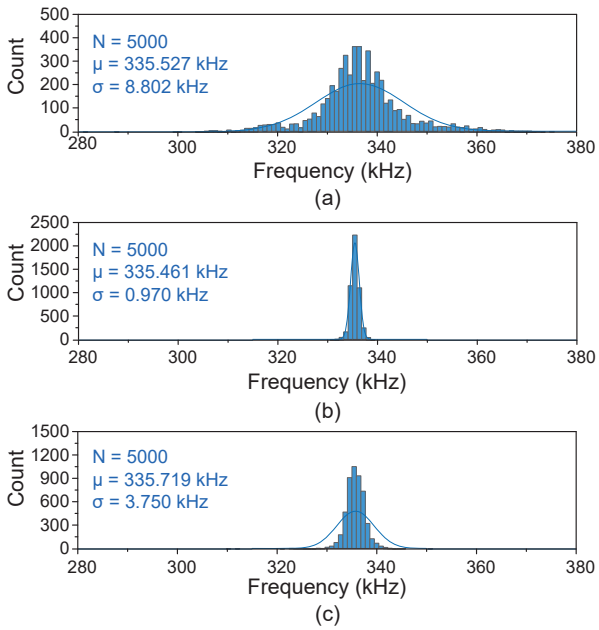

Figure 14: Measured effective frequency of the RX AFE output. The AFE output's frequency is calculated based on $f_{\text{ME,eff}} = (N_j - N_i)/T_{\text{ME}}$, where T_{ME} covers from the N_ith to the N_jth AFE output pulses. Tests were conducted at a 2-cm distance with different configurations of N_i and N_j: in (a), N_i is 9 and N_j is 10; in (b), N_i is 9 and N_j is 18; in (c), N_i is 9 and N_j is 22. An optimal configuration will minimize the frequency variation.

whose frequency is ideally the same as the ME backscattered field. The AFE circuit has a quiescent power dissipation of 84 mW.

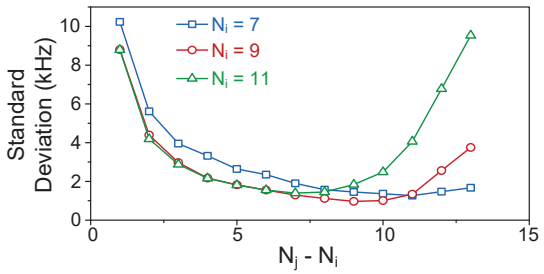

Figure 15: Standard deviation of the AFE output's effective frequency with different N_i and N_j. Tests were conducted at a 2-cm distance. The smallest σ is demonstrated when N_i equals to 9 and N_j equals to 18.

5.2.2 Digital Demodulation Circuit Design. The backscatter RX's digital backend employs frequency-to-digital conversion for uplink data demodulation. It uses several pulses of the AFE's output to build the demodulation window, transforming the LSK-induced frequency shift to a change of T_{ME} (see Figure 13 (c)). A counter is used to count the number of FPGA clock in the demodulation window to compute T_{ME}. When the ME transducer is connected with a capacitor, the backscattered signal's frequency decreases, resulting in a longer T_{ME}. Hence, by comparing T_{ME} with a predefined threshold T_{th}, LSK-modulated bits "1" and "0" can be recovered.

5.3 Design Optimization

As opposed to amplitude-shift-keying (ASK) requiring signal amplitude changes, the backscattered magnetic field's frequency change is almost independent of the channel quality, making it more robust to noise, interference, distance variations, and misalignment. Ideally, the frequency of the RX AFE's output should be the same as the backscattered magnetic field. In practice, the AFE-recovered pulses are subject to unavoidable frequency variations due to the circuit noise. With this concern, we included multiple pulses to calculate the effective frequency $f_{ME,eff}$ with alleviated variance. In Figure 13 (c), T_{ME} covers the time between the N_ith and the N_jth AFE output pulse to average the phase variation. The effective frequency of the backscattered signal $f_{ME,eff}$ is defined as $(N_j - N_i)/T_{ME}$. Measured results given in Figure 14 (a) and (b) demonstrate that using multiple pulses in effective frequency calculation can help reduce the frequency variance.

It's interesting to note that increasing N does not guarantee a lower frequency variance. The ME transducer voltage continuously decreases when the magnetic field turns off, making the ME backscatter signals a declining magnitude. Therefore, the later AFE output pulse have more considerable frequency variations due to the lower SNR. Figure 14 (c) shows a larger frequency variance than (b) because of the increase of N_j from 18 to 22. Since the TX coil has a ringing down behavior when the power amplifier turns off, for accurate frequency shift detection, we should process the signal sensed by the pick-up coil after the TX coil voltage disappears to decouple the applied magnetic field and the backscattered field, which means N_i should be large enough. Thus, there exists an optimal configuration for N_i and N_j to achieve the best performance. When N_i is too small, interference from the excitation field will affect the detection of resonance frequency change; with a larger N_j, the RX circuit wrestles with weaker backscattered signals. Both issues

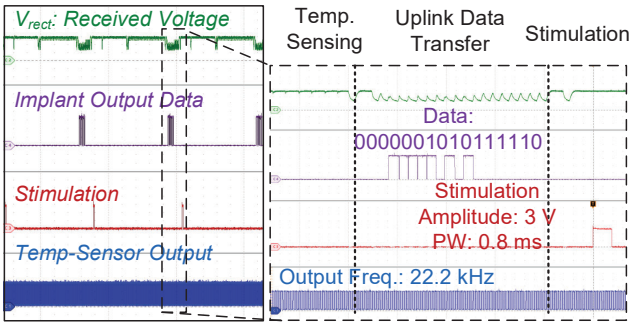

Figure 16: Measured operation waveforms of the implant. The magnetoelectrically powered and programmed implant continuously conducted temperature sensing, uplink data transfer, and stimulation. A zoom-in view shows the implant's temperature sensor output, uplink data output and stimulation pulse.

cause a lower SNR and hence a larger variation in the recovered pulse's frequency. As shown in Figure 15, the configuration that N_i is 9 and N_j is 18 minimizes the frequency variance.

6 EXPERIMENTAL RESULTS

We implemented a prototype system comprised of a custom ME transceiver (TRX) built with off-the-shelf components and an 8.2-mm^3 wireless implant integrating a 1.5-mm^2 ASIC chip, a 2×5×0.28-mm^3 ME transducer, and a 0.25-mm^3, 22-μF energy storage capacitor (see Figure 2). The ASIC is fabricated in commercial 180-nm complementary metal-oxide-semiconductor (CMOS) process.

6.1 System Functionality

The implant wirelessly receives > 1-mW power and 60-kbps downlink data through ME from the external TRX. The highest power transfer efficiency (PTE) of 4.3% is achieved with a 0-mm TRX-implant distance. When the distance is 2 cm, to generate a 3-V voltage (i.e., 2.8-mW maximum input power) in the implant's transducer, the power transmitting coil consumes 1.9 W, resulting in a peak PTE of 0.15%. The PTE is higher than the state-of-the-art mm-sized implants that are powered by inductive coupling [23, 30] and ultrasound [39]. The applied magnetic field to deliver this amount of power to 2 cm has a maximum strength of 2.4 mT, which is far below the 8-mT limit based on the IEEE standard C95.1-2019 [3, 18]. Figure 16 shows an example of the implant's operation, where the implant is programmed by the downlink data to sequentially conduct temperature sensing, uplink data transfer, and stimulation in one operating cycle. The embedded temperature sensor generates a clock signal with a temperature-dependent frequency, which is 22.2 kHz at the room temperature, as shown in the zoom-in views. Using frequency-to-digital conversion, the sensor output clock is converted into 16-bit uplink data. When the uplink bit is "1", the ASIC connects the ME transducer to the 120-pF load, leading to a resonance frequency shift and a slight reduction of the received voltage that does not interrupt the operation of the circuitry. After the uplink data transfer session, the circuit generates a programmed 3-V, 0.8-ms pulse for bio-stimulation.

The uplink data from the implant is transmitted to the external TRX through the ME backscatter with a maximum 8-kbps data rate. The waveform in Figure 17 gives an example of uplink data

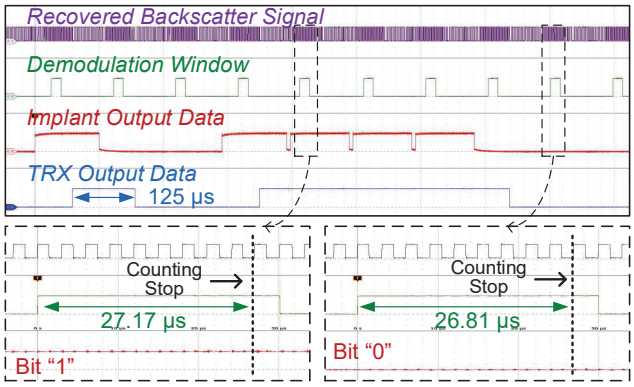

Figure 17: Measured waveforms of the ME backscatter communication. Uplink data from the implant was sent through ME backscatter and received by the external TRX. The implant modulated the frequency of backscattered signal through LSK. Different pulse widths were observed for bit "1" and "0", as shown in the zoom-in views.

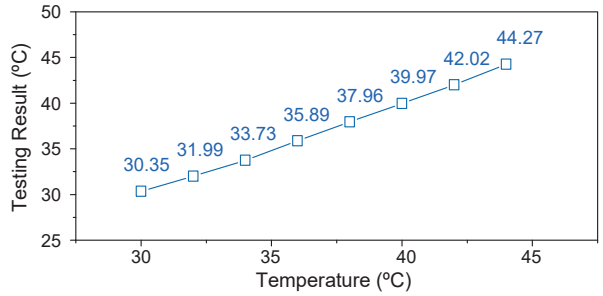

Figure 18: Measured temperature sensor error of the implant. The data are transmitted from the implant through the ME backscatter. The implant tested in a temperature chamber from 30 °C to 44 °C demonstrated a inaccuracy smaller than 0.35°C.

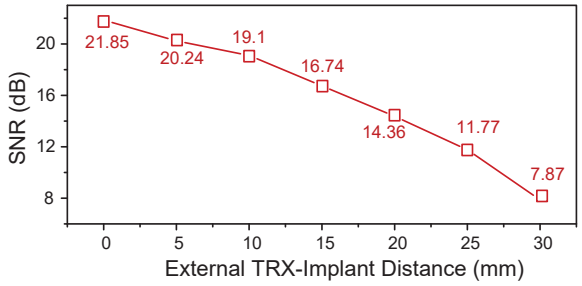

Figure 19: Measured ME backscatter SNR at various distances.

recovery in the external TRX. The ME backscattered signal is received by the pick-up coil and converted to digital pulses by the AFE circuit. Following the optimization presented in Section 5, the demodulation window of the TRX is between the 9th and the 18th pulses. The window's duration differs with different data due to the frequency change of the backscattered signal. In the examples shown in Figure 17, the demodulation window's duration is 27.17 µs when receiving bit "1" and reduces to 26.81 µs for bit "0".

Human temperature control plays a vital role in regulating metabolism and maintaining homeostasis [58]. Remote, accurate temperature measurement enabled by miniaturized wireless implants can

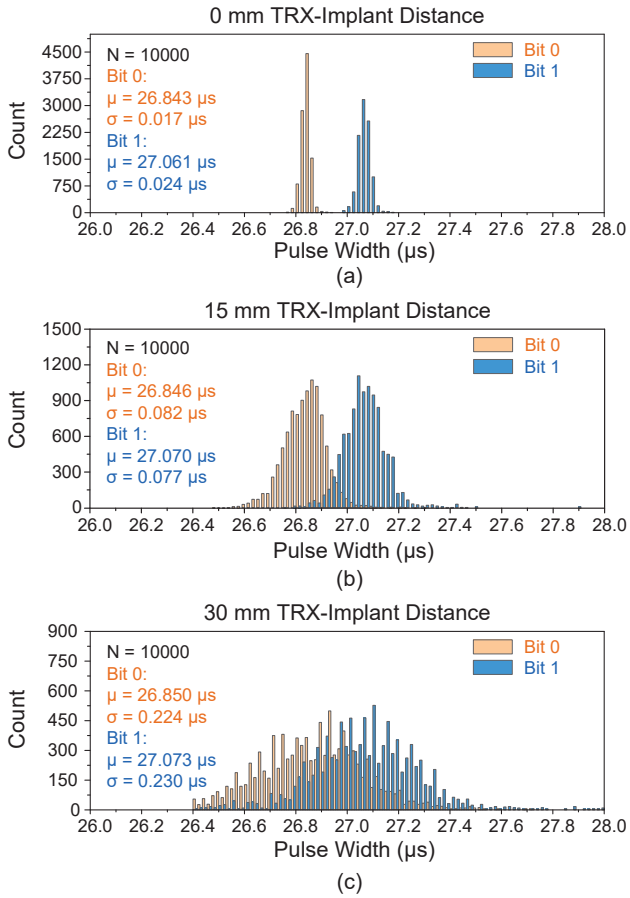

Figure 20: Distribution of pulse width for bit "1" and "0". Tests were conducted at different TRX-implant distances of (a) 0 mm; (b) 15 mm; and (c) 30 mm. As the TRX-implant distance increases, the standard deviations become larger.

lead to real-time thermal monitoring with high spatial resolution in deep tissue. [43]. To evaluate the proposed system's capability of wireless temperature sensing, we tested the ME implant in a temperature chamber from 30 °C to 44 °C. The implant transmits the sensing results through the ME backscatter to the external TRX. It achieves a < 0.35 °C inaccuracy in the testing temperature range (see Figure 18). The experiment also validates the implantable device's functionalities at different temperatures.

6.2 Magnetoelectric Backscatter Performance

The backscattered signal from a size-constrained implant is typically weak, particularly when the distance between TRX and implant is in centimeters. For example, in [1], the SNR of the 900-MHz RF backscatter using a 2-cm loop antenna in the implant is merely 6 dB at 10 cm. The FSK technique does not rely on signal amplitude changes, making it more robust to implantation uncertainties like varying distances and misalignment. However, due to the thermal noise in the TRX and environmental interference, the recovered backscatter signal unavoidably suffers from pulse width variations. This pulse width variation may introduce bit errors because the LSK-induced frequency change is merely 1%. We assessed the SNR

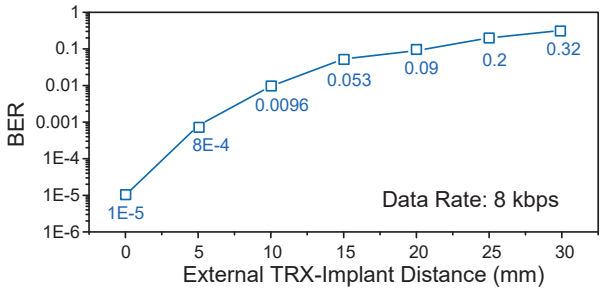

Figure 21: Measured BER versus the external TRX-implant distances with a data rate of 8 kbps.

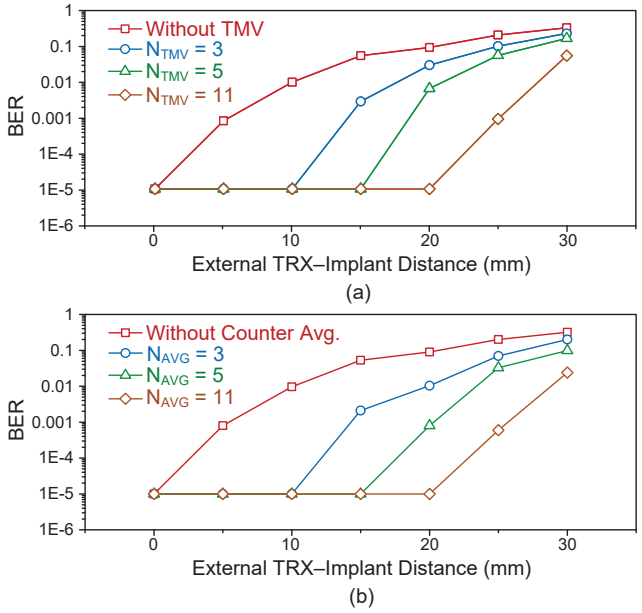

Figure 22: Techniques for ME backscatter bit error reduction. Tested BER with techniques of (a) output data temporal majority voting and (b) frequency counter averaging.

of ME backscatter at multiple TRX-implant distances. The SNR is measured at the TRX AFE's output since the pick-up coil coupled noise/interference and AFE circuit's thermal noise are the main noise sources. The SNR is measured to be 21.85 dB when the implant locates closely to the TRX (i.e. 0-mm distance), as shown in Figure 19. Increasing the distance between the implant and TRX leads to weaker backscattered signals in the pick-up coil, so the SNR reduces to 16.74 dB and 7.87 dB at 15-mm and 30-mm distances, respectively.

Received backscatter signal with lower SNR results in a larger variation of the recovered signal's pulse width, deteriorating the frequency-to-digital-based data demodulation. Figure 20 shows the pulse width distribution of measured 10,000 samples at different TRX-implant distances. While the mean values are consistent in these three cases, the standard deviations change considerably. At 0 mm, due to the small σ, no overlap of two distributions is observed; the 95-ns minimum time difference is much larger than the 3-ns demodulation resolution, which means bits can be easily distinguished (see Figure 20 (a). When the distance increases to 1.5 cm, σ becomes to 0.082 µs for bit "0" and 0.077 µs for bit "1", giving some non-distinguishable bit samples (see Figure 20 (b). As shown in Figure 20 (c), when the implant is 3 cm away from the TRX, the two distributions start to merge, making the data demodulation difficult. In the bit error tests, when the implant is at 0 mm, the BER is less than 1E-5. A BER of 9.6E-3 is achieved when transmitting the 8-kbps data over a 10-mm distance (see Figure 21). As the distance increases, the BER increases due to the decreasing SNR.

6.3 BER Enhancements

Reducing bit error is crucial for extending communication distance and enhancing system robustness. Increasing the uplink signal strength to increase SNR can effectively reduce data demodulation errors. However, in the ME backscatter, it may require higher TRX power to generate stronger excitation fields or a larger transducer size to store more mechanical energy. Here, based on the simple principle of repeating data transfers to average out noise, we implemented two digital methods in the external TRX to lessen bit errors at a given backscattered signal strength: temporal majority voting of received bit and averaging of frequency counter values.

6.3.1 Temporal Majority Voting of Output Data. Temporal majority voting (TMV) technique is widely used for stabilizing noisy binary outputs in circuits thanks to its simple implementation [32]. Specifically, an N-cycle TMV is implemented to reduce bit errors in ME backscatter in the following steps.

(1) Storing the digital data recovered by the TRX over N repeated uplink cycles;
(2) Summing the ith bit b_i of the stored data of each cycle and comparing the summation D_{i_TMV} with a threshold n, where $n = \frac{N-1}{2}$;
(3) If $D_{i\_TMV} > n$, setting D_{i_final} to "1", otherwise setting D_i to "0", where D_{i_final} is the ith bit in the final data.

As shown in Figure 22 (a), the TMV technique significantly improves the BER. By using a 5-cycle TMV, the BER is reduced from 0.053 to 1E-5 with a 15-mm TRX-implant distance while still achieving a 1.6-kbps effective data rate.

6.3.2 Frequency Counter Averaging. Averaging the demodulation circuit's counter values is an alternative method to process the repeated data transfers. The cycle counts of the received backscatter signal in a given demodulation window is used for time-to-digital conversion and data decoding. The counts are not constant because of pulse-width variations of the TRX's AFE-generated pulses. As a result of multi-cycle averaging, the counter value variations will be alleviated, leading to fewer bit errors. An experimental evaluation of this method is shown in Figure 22 (b). Compared to TMV, the counter value averaging shows higher effectiveness in reducing bit error, especially when the number of repeating cycles is large. For example, at a 20-mm distance, the 5-cycle counter value averaging achieves a BER of 8E-4, which is 6.3E-3 when utilizing the TMV.

Even though these methods reduce the effective data rate, they greatly improve the accuracy of data demodulation without the need for stronger backscattered signals. With a 5-cycle counter value averaging, a 1.6-kbps uplink data rate can be achieved with less than 1E-3 BER. The 2-cm TRX-implant distance is sufficient for neural stimulation and recording on the cortex [28], vagus nerve [50], and other peripheral nerves [27, 44], whose depths are

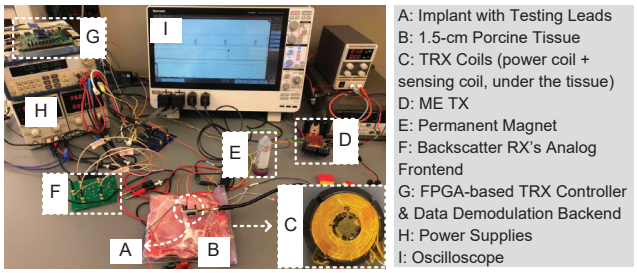

Figure 23: Illustration of the *ex-vivo* test. The porcine tissue used in the test is 1.5-cm thick, which covered the TRX's coils; the implant was placed on the surface of the tissue with testing leads for functionality monitoring.

within 2 cm from the skin surface. Potential applications also include electrocardiography sensing, temperature monitoring, heartbeat detection, and blood pressure measurement, which typically feature kHz or sub-kHz bandwidth at cm-scale depths [19, 62].

For applications requiring deeper implantation, various approaches are possible to improve the SNR and thus extend the ME backscatter's communication distance. A straightforward approach is to increase the voltage generated by the ME transducer. While the maximum voltage in the prototype implant is limited to 3.3 V by the standard CMOS, adopting a high-voltage CMOS process [5] will allow a higher induced voltage across the ME transducer to strengthen the backscattered signal. For example, our experiments show that a 2×5-mm^2 ME transducer with a 7-V output voltage enhances the backscattered signal's amplitude by 7.5 dB when compared with a 3.3-V transducer of the same size, extending the maximum TRX-implant distance to 3.6 cm where a < 1E-3 BER and a > 1kbps data rate are achieved. Alternatively, increasing the ME transducer's size will increase the energy stored in the ME material without requiring a stronger excitation field. By increasing the length from 5 to 7 mm, the 3-V ME transducer's backscattered signal is boosted by 5.6 dB, leading to a 1.2 cm improvement in communication range. Such an increase of transducer size will enlarge the implant's volume by merely 1.12-mm^3.

6.4 *Ex-Vivo* Tests

To evaluate the proposed system's performance in biological tissue, we performed *ex-vivo* tests with a porcine tissue of 1.5 cm thickness as a medium. The porcine tissue consisting of skin, fat and muscle was placed between the implantable device and the TRX coils (see Figure 23). The implants wirelessly received sufficient power, reliably operated and communicated with the external TRX during the testing. Pulse width distribution in uplink data demodulation is analyzed (see Figure 24). Compared to the measurements conducted in air with the same TRX-implant separation, the *ex-vivo* test show slightly increased standard deviations of pulse width, which are 0.097 µs for data "0" and 0.101 µs for data "1". This performance degradation is mainly caused by the path loss when the alternating magnetic field penetrates the tissue. However, it is worth noting that compared to high-frequency RF or inductive coupling, the 335-kHz magnetic field's energy loss inside tissue is much smaller since the tissue conductivity is much lower at this frequency (0.4 S/m at 335 kHz and 2 S/m at 2.4 GHz for muscle) [55]. BER was also

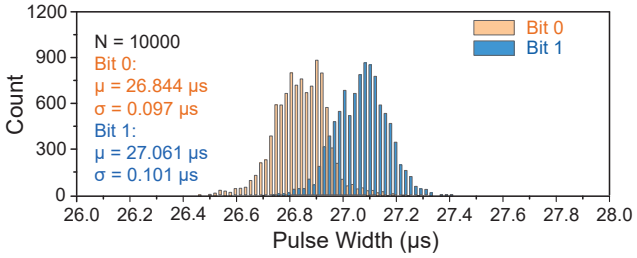

Figure 24: *Ex-vivo* tested pulse width distribution for bit "1" and "0".

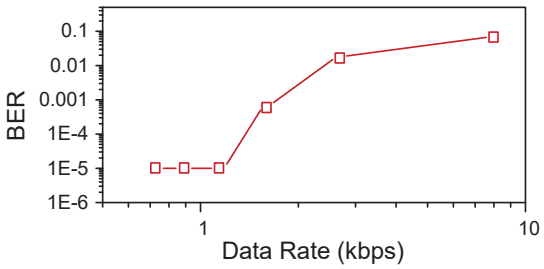

Figure 25: *Ex-vivo* tested BER versus data rate. The counter value averaging technique is used to improve the accuracy of data demodulation.

evaluated *ex vivo* with the results shown in Figure 21. The counter output averaging technique was utilized for reducing bit errors. The system achieves lower than 1E-3 BER at a 1.6-kbps effective data rate with the 1.5-cm porcine tissue.

7 RELATED WORK

7.1 Magnetoelectrically Powered and Controlled Bio-Implants

Magnetoelectrics are being explored to remotely deliver power and data to the implanted devices because they have considerable advantages in the context of power transfer through the human body, including high efficiency, good misalignment tolerance, and significantly alleviated tissue absorption concerns [3, 6, 17, 45, 59–61]. [45] reported a magnetoelectrically powered device for fully implanted nerve stimulation. [59] proven ME's compatibility with CMOS chip and capability of wireless data transfer in downlink. In the wireless implant network developed by [60], multiple implants are powered and individually programmed by a single ME TX for coordinated multisite stimulation. Recently, [6] achieved minimally invasive endovascular nerve stimulation with a ME neurostimulator. Furthermore, [3] demonstrated a wearable ME power transfer system with a battery-powered transmitter assembled in a belt.

Despite significant progress made to develop ME technologies and ME bio-implants, solutions for ME backscatter to wirelessly transmit data from implants were missing. The absence of uplink communication impedes [3, 6, 45, 59, 60] from being applied for instantaneous physiologic monitoring and closed-loop physiology control. While combing ME with other modalities, such as inductive coupling, as a hybrid wireless scheme is doable [61], it requires an additional antenna or transducer, which makes the device integration and miniaturization more challenging. For the first time, ME power transfer and bi-directional telemetries are simultaneously

achieved in this work. The novel ME backscatter technique opens up a new path for the realization of highly efficient uplink telemetry in implantable systems that takes advantage of the ME power transfer.

7.2 Backscatter Communication in Bio-Implants

7.2.1 RF and Inductive Backscatter. Thanks to the excellent electronic circuit compatibility and functional flexibility, RF [1, 10, 30, 36] and inductive-coupling-based [33, 37, 51, 57] mechanisms have become the most popular backscatter techniques. They exploit the coupling between the antennas/coils of the external TRX and the implant in an electromagnetic field: the implant antenna/coil's load change can result in a voltage or current change in the external TRX's antenna/coil. The implant's circuits usually conduct load-shift-keying modulation to encode information on top of the carrier signal. With a high carrier frequency, RF or inductive backscatter can support a wide bandwidth to transmit high-speed data. [1, 30, 51, 57] working at hundreds of megahertz or gigahertz achieve uplink data rates higher than 1 Mbps. Higher frequencies, however, may raise more concerns about tissue absorption and stricter constraints on the maximum carrier field strength [18, 47]. While a large distance (> 10 cm) was achieved by a self-adapted resonant antenna [1], the antenna has a dimension of around 2 cm, limiting the implant's miniaturization. With smaller antenna or coil sizes, the largest powering and communication ranges may dramatically decrease due to weak coupling. For instance, devices equipped with a 1.2-mm [51] or 0.5-mm coil [57] operate with a implantation depth smaller than 5 mm. Therefore, trade-offs between carrier field strength and data rate, as well as distance versus implant size, can constrain the design of power transfer and communication channels using RF or inductive coupling.

7.2.2 Ultrasonic Backscatter. Ultrasound has gained increasing attention as a power source for bio-implants in recent years. Compared to RF signal and inductive coupling, ultrasound waves are able to transmit at a lower frequency with a smaller wavelength for alleviated safety limits and more efficient coupling to the mm-sized devices [39, 42]. Ultrasonic implants can modulate echo magnitude in either a digital [43, 48] or analog [14, 42] manner by adjusting the electric properties of their piezoelectric transducers. Because ultrasound relies on propagating waves, it can transmit over centimeter-long distances. [48] demonstrated 2.6-cm-deep oxygen sensing in vivo with a 4.5-mm^3 implant, and [14] achieved a maximum TRX-implant separation of 5 cm in saline. Another improvement achieved by ultrasound is device miniaturization. Because of the wavelength below one millimeter, the ultrasonic implants appeared scalable down to sub-mm^3 sizes [14, 43]. However, the relatively low carrier frequency and acoustic waves' time of flight may limit the data rates, which are 1 kbps in [43] and 35 kbps in [14]. More importantly, an inherent bottleneck in ultrasonic powering and communication results from substantial acoustic impedance mismatches between different materials, which dissipate or reflect sound waves. For this reason, the external TRXs require to be placed in contact with skin with gels to decrease air-skin impedance mismatch [39, 42, 43, 48]. Similarly, it is challenging to use ultrasound to deliver signals through the bone when implanting the devices within the brain [7].

8 CONCLUSION

We designed a wireless implantable system exploiting magnetoelectric (ME) materials for wireless power and bi-directional data transfers. The ME backscatter leveraging the converse magnetostriction effect enables efficient uplink telemetry from the 8.2-mm^3 implant to the external TRX. An 1.5-mm^2 ASIC chip fabricated in 180-nm CMOS process switches the capacitive load of a 2×5-mm^2 ME thin-film transducer to shift its resonance frequency for uplink data modulation. By detecting the frequency change of the backscattered magnetic field with a novel frequency-to-digital conversion scheme, the external TRX successfully recovered the uplink data at a cm-scale distance. To the best of our knowledge, this is the first demonstration of ME backscatter communication for bioelectronic implantable devices, as well as the first mm-scale wireless and batteryless bio-implant that uses a single ME transducer for efficient wireless powering and bidirectional communication.

Our prototype system achieves an 8-kbps maximum data rate in uplink through the ME backscatter. After error reduction techniques, a BER smaller than 1E-3 is demonstrated at 2 cm implant-TRX distance while achieving > 1-kbps data rate. The system's performance was validated at multiple temperatures and *ex vivo* with a 1.5-cm porcine tissue, proving its operation robustness and biological tissue compatibility. The presented technology is promising for a wide range of bioelectronic medicine applications that require bi-directional communication and wireless power transfer, such as closed-loop neuromodulation and real-time physiology monitoring.

ACKNOWLEDGEMENT

We thank our anonymous shepherd and reviewers for their constructive comments. This project is funded in part by the National Science Foundation ASCENT Program ECCS-2023849 and by the Defense Advanced Research Projects Agency (DARPA) under agreement number FA8650-21-2-7119. The views, opinions and/or findings expressed are those of the author and should not be interpreted as representing the official views or policies of the Department of Defense or the U.S. Government. JTR and KY have an equity stake in Motif Neurotech, Inc.

REFERENCES

[1] Mohamed R. Abdelhamid, Ruicong Chen, Joonhyuk Cho, Anantha P. Chandrakasan, and Fadel Adib. 2020. Self-reconfigurable micro-implants for cross-tissue wireless and batteryless connectivity. In *Proceedings of the 26th Annual International Conference on Mobile Computing and Networking*. ACM, London United Kingdom, 1–14. https://doi.org/10.1145/3372224.3419216

[2] Dukju Ahn and Maysam Ghovanloo. 2016. Optimal Design of Wireless Power Transmission Links for Millimeter-Sized Biomedical Implants. *IEEE Transactions on Biomedical Circuits and Systems* 10, 1 (Feb. 2016), 125–137. https://doi.org/10.1109/TBCAS.2014.2370794

[3] Fatima T. Alrashdan, Joshua C. Chen, Amanda Singer, Benjamin W. Avants, Kaiyuan Yang, and Jacob T. Robinson. 2021. Wearable wireless power systems for 'ME-BIT' magnetoelectric-powered bio implants. *Journal of Neural Engineering* 18, 4 (July 2021), 045011. https://doi.org/10.1088/1741-2552/ac1178 Publisher: IOP Publishing.

[4] Alex Burton, Sofian N. Obaid, Abraham Vázquez-Guardado, Matthew B. Schmit, Tucker Stuart, Le Cai, Zhiyuan Chen, Irawati Kandela, Chad R. Haney, Emily A. Waters, Haijiang Cai, John A. Rogers, Luyao Lu, and Philipp Gutruf. 2020. Wireless, battery-free subdermally implantable photometry systems for chronic

recording of neural dynamics. *Proceedings of the National Academy of Sciences* 117, 6 (Feb. 2020), 2835–2845. https://doi.org/10.1073/pnas.1920073117

[5] Jayant Charthad, Ting Chia Chang, Zhaokai Liu, Ahmed Sawaby, Marcus J. Weber, Sam Baker, Felicity Gore, Stephen A. Felt, and Amin Arbabian. 2018. A mm-Sized Wireless Implantable Device for Electrical Stimulation of Peripheral Nerves. *IEEE Transactions on Biomedical Circuits and Systems* 12, 2 (April 2018), 257–270. https://doi.org/10.1109/TBCAS.2018.2799623

[6] Joshua C. Chen, Peter Kan, Zhanghao Yu, Fatima Alrashdan, Roberto Garcia, Amanda Singer, C. S. Edwin Lai, Ben Avants, Scott Crosby, Zhongxi Li, Boshuo Wang, Michelle M. Felicella, Ariadna Robledo, Angel V. Peterchev, Stefan M. Goetz, Jeffrey D. Hartgerink, Sunil A. Sheth, Kaiyuan Yang, and Jacob T. Robinson. 2022. A wireless millimetric magnetoelectric implant for the endovascular stimulation of peripheral nerves. *Nature Biomedical Engineering* (March 2022), 1–11. https://doi.org/10.1038/s41551-022-00873-7 Publisher: Nature Publishing Group.

[7] G. T. Clement, P. J. White, and K. Hynynen. 2004. Enhanced ultrasound transmission through the human skull using shear mode conversion. *The Journal of the Acoustical Society of America* 115, 3 (March 2004), 1356–1364. https://doi.org/10.1121/1.1645610 Publisher: Acoustical Society of America.

[8] Marcelo J. Dapino, Ralph C. Smith, Frederick T. Calkins, and Alison B. Flatau. 2002. A Coupled Magnetomechanical Model for Magnetostrictive Transducers and its Application to Villari-Effect Sensors. *Journal of Intelligent Material Systems and Structures* 13, 11 (Nov. 2002), 737–747. https://doi.org/10.1177/1045389X02013011005 Publisher: SAGE Publications Ltd STM.

[9] Cunzheng Dong, Yifan He, Menghui Li, Cheng Tu, Zhaoqiang Chu, Xianfeng Liang, Huaihao Chen, Yuyi Wei, Mohsen Zaeimbashi, Xinjun Wang, Hwaider Lin, Yuan Gao, and Nian X. Sun. 2020. A Portable Very Low Frequency (VLF) Communication System Based on Acoustically Actuated Magnetoelectric Antennas. *IEEE Antennas and Wireless Propagation Letters* 19, 3 (March 2020), 398–402. https://doi.org/10.1109/LAWP.2020.2968604

[10] Xiaoran Fan, Longfei Shangguan, Richard Howard, Yanyong Zhang, Yao Peng, Jie Xiong, Yunfei Ma, and Xiang-Yang Li. 2020. Towards flexible wireless charging for medical implants using distributed antenna system. In *Proceedings of the 26th Annual International Conference on Mobile Computing and Networking*. ACM, London United Kingdom, 1–15. https://doi.org/10.1145/3372224.3380899

[11] Z. Fang, S. G. Lu, F. Li, S. Datta, Q. M. Zhang, and M. El Tahchi. 2009. Enhancing the magnetoelectric response of Metglas/polyvinylidene fluoride laminates by exploiting the flux concentration effect. *Applied Physics Letters* 95, 11 (Sept. 2009), 112903. https://doi.org/10.1063/1.3231614

[12] Kyriaki Fotopoulou and Brian W. Flynn. 2011. Wireless Power Transfer in Loosely Coupled Links: Coil Misalignment Model. *IEEE Transactions on Magnetics* 47, 2 (Feb. 2011), 416–430. https://doi.org/10.1109/TMAG.2010.2093534

[13] Daniel K. Freeman, Jonathan M. O'Brien, Parshant Kumar, Brian Daniels, Reed A. Irion, Louis Shraytah, Brett K. Ingersoll, Andrew P. Magyar, Andrew Czarnecki, Jesse Wheeler, Jonathan R. Coppeta, Michael P. Abban, Ronald Gatzke, Shelley I. Fried, Seung Woo Lee, Amy E. Duwel, Jonathan J. Bernstein, Alik S. Widge, Ana Hernandez-Reynoso, Aswini Kanneganti, Mario I. Romero-Ortega, and Stuart F. Cogan. 2017. A Sub-millimeter, Inductively Powered Neural Stimulator. *Front. Neurosci.* 11 (2017). https://doi.org/10.3389/fnins.2017.00659

[14] Mohammad Meraj Ghanbari, David K. Piech, Konlin Shen, Sina Faraji Alamouti, Cem Yalcin, Benjamin C. Johnson, Jose M. Carmena, Michel M. Maharbiz, and Rikky Muller. 2019. A Sub-mm3 Ultrasonic Free-Floating Implant for Multi-Mote Neural Recording. *IEEE Journal of Solid-State Circuits* 54, 11 (Nov. 2019), 3017–3030. https://doi.org/10.1109/JSSC.2019.2936303

[15] Craig A. Grimes, Somnath C. Roy, Sanju Rani, and Qingyun Cai. 2011. Theory, Instrumentation and Applications of Magnetoelastic Resonance Sensors: A Review. *Sensors (Basel, Switzerland)* 11, 3 (March 2011), 2809–2844. https://doi.org/10.3390/s110302809

[16] Peter R. Hoskins, Kevin Martin, and Abigail Thrush. 2010. *Diagnostic Ultrasound: Physics and Equipment.* Cambridge University Press.

[17] Sujay Hosur, Rammohan Sriramdas, Sumanta Kumar Karan, Na Liu, Shashank Priya, and Mehdi Kiani. 2021. A Comprehensive Study on Magnetoelectric Transducers for Wireless Power Transfer using Low-Frequency Magnetic Fields. *IEEE Transactions on Biomedical Circuits and Systems* (2021), 1–1. https://doi.org/10.1109/TBCAS.2021.3118981

[18] IEEE. 2019. IEEE Standard for Safety Levels with Respect to Human Exposure to Electric, Magnetic, and Electromagnetic Fields, 0 Hz to 300 GHz. *IEEE Std C95.1-2019 (Revision of IEEE Std C95.1-2005/ Incorporates IEEE Std C95.1-2019/Cor 1-2019)* (Oct. 2019), 1–312. https://doi.org/10.1109/IEEESTD.2019.8859679

[19] Mohd Noor Islam and Mehmet R. Yuce. 2016. Review of Medical Implant Communication System (MICS) band and network. *ICT Express* 2, 4 (Dec. 2016), 188–194. https://doi.org/10.1016/j.icte.2016.08.010

[20] Vikram Iyer, Vamsi Talla, Bryce Kellogg, Shyamnath Gollakota, and Joshua Smith. 2016. Inter-Technology Backscatter: Towards Internet Connectivity for Implanted Devices. In *Proceedings of the 2016 ACM SIGCOMM Conference*. ACM, Florianopolis Brazil, 356–369. https://doi.org/10.1145/2934872.2934894

[21] Yaoyao Jia, Ulkuhan Guler, Yen-Pang Lai, Yan Gong, Arthur Weber, Wen Li, and Maysam Ghovanloo. 2020. 26.8 A Trimodal Wireless Implantable Neural Interface System-on-Chip. In *2020 IEEE International Solid- State Circuits Conference - (ISSCC)*. 414–416. https://doi.org/10.1109/ISSCC19947.2020.9063065

[22] Mohammad Javad Karimi, Alexandre Schmid, and Catherine Dehollain. 2021. Wireless Power and Data Transmission for Implanted Devices via Inductive Links: A Systematic Review. 21, 6 (March 2021), 7145–7161. https://doi.org/10.1109/JSEN.2021.3049918

[23] Adam Khalifa, Yuxin Liu, Yasha Karimi, Qihong Wang, Adebayo Eisape, Milutin Stanaćević, Nitish Thakor, Zhenan Bao, and Ralph Etienne-Cummings. 2019. The Microbead: A 0.009 mm3 Implantable Wireless Neural Stimulator. *IEEE Transactions on Biomedical Circuits and Systems* 13, 5 (Oct. 2019), 971–985. https://doi.org/10.1109/TBCAS.2019.2939014

[24] Nai-Chung Kuo, Bo Zhao, and Ali M. Niknejad. 2016. Inductive Wireless Power Transfer and Uplink Design for a CMOS Tag With 0.01 mm2 Coil Size. *IEEE Microwave and Wireless Components Letters* 26, 10 (Oct. 2016), 852–854. https://doi.org/10.1109/LMWC.2016.2605440

[25] Yat-Hei Lam, Wing-Hung Ki, and Chi-Ying Tsui. 2006. Integrated Low-Loss CMOS Active Rectifier for Wirelessly Powered Devices. *IEEE Transactions on Circuits and Systems II: Express Briefs* 53, 12 (Dec. 2006), 1378–1382. https://doi.org/10.1109/TCSII.2006.885400

[26] David W. Landgren, Kevin R. Cook, Daniel J. P. Dykes, Jonathan Perez, Phillip R. Bowden, and Kenneth W. Allen. 2017. A wideband mmWave antenna element with an unbalanced feed. In *2017 IEEE National Aerospace and Electronics Conference (NAECON)*. 209–212. https://doi.org/10.1109/NAECON.2017.8268771

[27] Byunghun Lee, Mukhesh K. Koripalli, Yaoyao Jia, Joshua Acosta, M. S. E. Sendi, Yoonsu Choi, and Maysam Ghovanloo. 2018. An Implantable Peripheral Nerve Recording and Stimulation System for Experiments on Freely Moving Animal Subjects. *Scientific Reports* 8, 1 (Dec. 2018), 6115. https://doi.org/10.1038/s41598-018-24465-1

[28] Jihun Lee, Vincent Leung, Ah-Hyoung Lee, Jiannan Huang, Peter Asbeck, Patrick P. Mercier, Stephen Shellhammer, Lawrence Larson, Farah Laiwalla, and Arto Nurmikko. 2021. Neural recording and stimulation using wireless networks of microimplants. *Nature Electronics* 4, 8 (Aug. 2021), 604–614. https://doi.org/10.1038/s41928-021-00631-8 Number: 8 Publisher: Nature Publishing Group.

[29] Sunwoo Lee, Alejandro Javier Cortese, Aasta Parin Gandhi, Elizabeth Rose Agger, Paul L. McEuen, and Alyosha Christopher Molnar. 2018. A 250 m × 57 m Microscale Opto-electronically Transduced Electrodes (MOTEs) for Neural Recording. *IEEE Transactions on Biomedical Circuits and Systems* 12, 6 (Dec. 2018), 1256–1266. https://doi.org/10.1109/TBCAS.2018.2876069

[30] Vincent W. Leung, Lingxiao Cui, Sravya Alluri, Jihun Lee, Jiannan Huang, Ethan Mok, Steven Shellhammer, Ramesh Rao, Peter Asbeck, Patrick P. Mercier, Lawrence Larson, Arto Nurmikko, and Farah Laiwalla. 2019. Distributed Microscale Brain Implants with Wireless Power Transfer and Mbps Bi-directional Networked Communications. In *2019 IEEE Custom Integrated Circuits Conference (CICC)*. 1–4. https://doi.org/10.1109/CICC.2019.8780289

[31] Vincent W. Leung, Jihun Lee, Siwei Li, Siyuan Yu, Chester Kilfovle, Lawrence Larson, Arto Nurmikko, and Farah Laiwalla. 2018. A CMOS Distributed Sensor System for High-Density Wireless Neural Implants for Brain-Machine Interfaces. In *ESSCIRC 2018 - IEEE 44th European Solid State Circuits Conference (ESSCIRC)*. 230–233. https://doi.org/10.1109/ESSCIRC.2018.8494335

[32] Dai Li and Kaiyuan Yang. 2020. A Self-Regulated and Reconfigurable CMOS Physically Unclonable Function Featuring Zero-Overhead Stabilization. *IEEE J. Solid-State Circuits* 55, 1 (Jan. 2020), 98–107. https://doi.org/10.1109/JSSC.2019.2938133

[33] Xing Li, Chi-Ying Tsui, and Wing-Hung Ki. 2015. A 13.56 MHz Wireless Power Transfer System With Reconfigurable Resonant Regulating Rectifier and Wireless Power Control for Implantable Medical Devices. *IEEE Journal of Solid-State Circuits* 50, 4 (April 2015), 978–989. https://doi.org/10.1109/JSSC.2014.2387832

[34] Jongyup Lim, Eunseong Moon, Michael Barrow, Samuel R. Nason, Paras R. Patel, Parag G. Patil, Sechang Oh, Inhee Lee, Hun-Seok Kim, Dennis Sylvester, David Blaauw, Cynthia A. Chestek, Jamie Phillips, and Taekwang Jang. 2020. A 0.19×0.17mm2 Wireless Neural Recording IC for Motor Prediction with Near-Infrared-Based Power and Data Telemetry. In *2020 IEEE International Solid- State Circuits Conference - (ISSCC)*. 416–418. https://doi.org/10.1109/ISSCC19947.2020.9063005

[35] Vincent Liu, Vamsi Talla, and Shyamnath Gollakota. 2014. Enabling instantaneous feedback with full-duplex backscatter. In *Proceedings of the 20th annual international conference on Mobile computing and networking*. ACM, Maui Hawaii USA, 67–78. https://doi.org/10.1145/2639108.2639136

[36] Yunfei Ma, Zhihong Luo, Christoph Steiger, Giovanni Traverso, and Fadel Adib. 2018. Enabling deep-tissue networking for miniature medical devices. In *Proceedings of the 2018 Conference of the ACM Special Interest Group on Data Communication (SIGCOMM '18)*. Association for Computing Machinery, New York, NY, USA, 417–431. https://doi.org/10.1145/3230543.3230566

[37] Soumyajit Mandal and Rahul Sarpeshkar. 2008. Power-Efficient Impedance-Modulation Wireless Data Links for Biomedical Implants. *IEEE Transactions on Biomedical Circuits and Systems* 2, 4 (Dec. 2008), 301–315. https://doi.org/10.1109/TBCAS.2008.2005295

[38] Kate L Montgomery, Alexander J Yeh, John S Ho, Vivien Tsao, Shrivats Mohan Iyer, Logan Grosenick, Emily A Ferenczi, Yuji Tanabe, Karl Deisseroth, Scott L Delp, and Ada S Y Poon. 2015. Wirelessly powered, fully internal optogenetics for brain, spinal and peripheral circuits in mice. *Nature Methods* 12, 10 (Oct. 2015), 969–974. https://doi.org/10.1038/nmeth.3536

[39] David K. Piech, Benjamin C. Johnson, Konlin Shen, M. Meraj Ghanbari, Ka Yiu Li, Ryan M. Neely, Joshua E. Kay, Jose M. Carmena, Michel M. Maharbiz, and Rikky Muller. 2020. A wireless millimetre-scale implantable neural stimulator with ultrasonically powered bidirectional communication. *Nature Biomedical Engineering* 4, 2 (Feb. 2020), 207–222. https://doi.org/10.1038/s41551-020-0518-9

[40] Richard C. Pinnell, Anne Pereira de Vasconcelos, Jean C. Cassel, and Ulrich G. Hofmann. 2018. A Miniaturized, Programmable Deep-Brain Stimulator for Group-Housing and Water Maze Use. *Front. Neurosci.* 12 (2018). https://doi.org/10.3389/fnins.2018.00231

[41] Tyrel Rupp, Binh Duc Truong, Shane Williams, and Shad Roundy. 2019. Magnetoelectric Transducer Designs for Use as Wireless Power Receivers in Wearable and Implantable Applications. *Materials* 12, 3 (Feb. 2019), 512. https://doi.org/10.3390/ma12030512

[42] Dongjin Seo, Ryan M. Neely, Konlin Shen, Utkarsh Singhal, Elad Alon, Jan M. Rabaey, Jose M. Carmena, and Michel M. Maharbiz. 2016. Wireless Recording in the Peripheral Nervous System with Ultrasonic Neural Dust. *Neuron* 91, 3 (Aug. 2016), 529–539. https://doi.org/10.1016/j.neuron.2016.06.034

[43] Chen Shi, Victoria Andino-Pavlovsky, Stephen A. Lee, Tiago Costa, Jeffrey Elloian, Elisa E. Konofagou, and Kenneth L. Shepard. 2021. Application of a sub–0.1-mm ^{3} implantable mote for in vivo real-time wireless temperature sensing. *Sci. Adv.* 7, 19 (May 2021), eabf6312. https://doi.org/10.1126/sciadv.abf6312

[44] Malin Silverå Ejneby, Marie Jakešová, Jose J. Ferrero, Ludovico Migliaccio, Ihor Sahalianov, Zifang Zhao, Magnus Berggren, Dion Khodagholy, Vedran Đerek, Jennifer N. Gelinas, and Eric Daniel Głowacki. 2022. Chronic electrical stimulation of peripheral nerves via deep-red light transduced by an implanted organic photocapacitor. *Nature Biomedical Engineering* 6, 6 (June 2022), 741–753. https://doi.org/10.1038/s41551-021-00817-7

[45] Amanda Singer, Shayok Dutta, Eric Lewis, Ziying Chen, Joshua C. Chen, Nishant Verma, Benjamin Avants, Ariel K. Feldman, John O'Malley, Michael Beierlein, Caleb Kemere, and Jacob T. Robinson. 2020. Magnetoelectric Materials for Miniature, Wireless Neural Stimulation at Therapeutic Frequencies. *Neuron* (June 2020). https://doi.org/10.1016/j.neuron.2020.05.019

[46] Amanda Singer and Jacob T. Robinson. 2021. Wireless Power Delivery Techniques for Miniature Implantable Bioelectronics. *Advanced Healthcare Materials* 10, 17 (2021), 2100664. https://doi.org/10.1002/adhm.202100664 _eprint: https://onlinelibrary.wiley.com/doi/pdf/10.1002/adhm.202100664.

[47] Nima Soltani, Maged ElAnsary, Jianxiong Xu, José Sales Filho, and Roman Genov. 2021. Safety-Optimized Inductive Powering of Implantable Medical Devices: Tutorial and Comprehensive Design Guide. *IEEE Transactions on Biomedical Circuits and Systems* 15, 6 (Dec. 2021), 1354–1367. https://doi.org/10.1109/TBCAS.2021.3125618

[48] Soner Sonmezoglu, Jeffrey R. Fineman, Emin Maltepe, and Michel M. Maharbiz. 2021. Monitoring deep-tissue oxygenation with a millimeter-scale ultrasonic implant. *Nature Biotechnology* 39, 7 (July 2021), 855–864. https://doi.org/10.1038/s41587-021-00866-y Number: 7 Publisher: Nature Publishing Group.

[49] Jingxiang Su, Florian Niekiel, Simon Fichtner, Christine Kirchhof, Dirk Meyners, Eckhard Quandt, Bernhard Wagner, and Fabian Lofink. 2020. Frequency tunable resonant magnetoelectric sensors for the detection of weak magnetic field. *Journal of Micromechanics and Microengineering* 30, 7 (May 2020), 075009. https://doi.org/10.1088/1361-6439/ab8dd0 Publisher: IOP Publishing.

[50] Yuji Tanabe, John S. Ho, Jiayin Liu, Song-Yan Liao, Zhe Zhen, Stephanie Hsu, Chika Shuto, Zi-Yi Zhu, Andrew Ma, Christopher Vassos, Peter Chen, Hung Fat Tse, and Ada S. Y. Poon. 2017. High-performance wireless powering for peripheral nerve neuromodulation systems. *PLOS ONE* 12, 10 (Oct. 2017), e0186698. https://doi.org/10.1371/journal.pone.0186698

[51] Jordan Thimot, Kukjoo Kim, Chen Shi, and Kenneth L. Shepard. 2020. A 27-Mbps, 0.08-mm3 CMOS Transceiver with Simultaneous Near-field Power Transmission and Data Telemetry for Implantable Systems. In *2020 IEEE Custom Integrated Circuits Conference (CICC)*. 1–4. https://doi.org/10.1109/CICC48029.2020.9075888

[52] Binh Duc Truong and Shad Roundy. 2020. Experimentally validated model and power optimization of a magnetoelectric wireless power transfer system in free-free configuration. *Smart Mater. Struct.* 29, 8 (Aug. 2020), 085053. https://doi.org/10.1088/1361-665X/ab90a2

[53] Binh Duc Truong, Shane Williams, and Shad Roundy. 2019. Experimentally validated model and analytical investigations on power optimization for piezoelectric-based wireless power transfer systems. *Journal of Intelligent Material Systems and Structures* 30, 16 (Sept. 2019), 2464–2477. https://doi.org/10.1177/1045389X19862383 Publisher: SAGE Publications Ltd STM.

[54] H. B. Wang and Z. H. Feng. 2013. A Highly Sensitive Magnetometer Based on the Villari Effect. *IEEE Transactions on Magnetics* 49, 4 (April 2013), 1327–1333. https://doi.org/10.1109/TMAG.2012.2220559

[55] Erda Wen, Daniel F. Sievenpiper, and Patrick P. Mercier. 2022. Channel Characterization of Magnetic Human Body Communication. *IEEE Transactions on Biomedical Engineering* 69, 2 (Feb. 2022), 569–579. https://doi.org/10.1109/TBME.2021.3101766

[56] Kaiyuan Yang, Qing Dong, Wanyeong Jung, Yiqun Zhang, Myungjoon Choi, David Blaauw, and Dennis Sylvester. 2017. 9.2 A 0.6nJ 0.22/+0.19°C inaccuracy temperature sensor using exponential subthreshold oscillation dependence. In *2017 IEEE International Solid-State Circuits Conference (ISSCC)*. 160–161. https://doi.org/10.1109/ISSCC.2017.7870310 ISSN: 2376-8606.

[57] D. Yeager, W. Biederman, N. Narevsky, E. Alon, and J. Rabaey. 2012. A fully-integrated 10.5μW miniaturized (0.125mm2) wireless neural sensor. In *2012 Symposium on VLSI Circuits (VLSIC)*. 72–73. https://doi.org/10.1109/VLSIC.2012.6243795 ISSN: 2158-5636.

[58] Tomoyuki Yokota, Yusuke Inoue, Yuki Terakawa, Jonathan Reeder, Martin Kaltenbrunner, Taylor Ware, Kejia Yang, Kunihiko Mabuchi, Tomohiro Murakawa, Masaki Sekino, Walter Voit, Tsuyoshi Sekitani, and Takao Someya. 2015. Ultraflexible, large-area, physiological temperature sensors for multipoint measurements. *Proceedings of the National Academy of Sciences* 112, 47 (Nov. 2015), 14533–14538. https://doi.org/10.1073/pnas.1515650112

[59] Zhanghao Yu, Joshua C. Chen, Fatima T. Alrashdan, Benjamin W. Avants, Yan He, Amanda Singer, Jacob T. Robinson, and Kaiyuan Yang. 2020. MagNI: A Magnetoelectrically Powered and Controlled Wireless Neurostimulating Implant. *IEEE Transactions on Biomedical Circuits and Systems* 14, 6 (Dec. 2020), 1241–1252. https://doi.org/10.1109/TBCAS.2020.3037862

[60] Zhanghao Yu, Joshua C. Chen, Yan He, Fatima T. Alrashdan, Benjamin W. Avants, Amanda Singer, Jacob T. Robinson, and Kaiyuan Yang. 2022. Magnetoelectric Bio-Implants Powered and Programmed by a Single Transmitter for Coordinated Multisite Stimulation. *IEEE Journal of Solid-State Circuits* 57, 3 (March 2022), 818–830. https://doi.org/10.1109/JSSC.2021.3129993

[61] Zhanghao Yu, Wei Wang, Joshua C. Chen, Zhiyu Chen, Yan He, Amanda Singer, Jacob T. Robinson, and Kaiyuan Yang. 2022. A Wireless Network of 8.8-mm3 Bio-Implants Featuring Adaptive Magnetoelectric Power and Multi-Access Bidirectional Telemetry. In *2022 IEEE Radio Frequency Integrated Circuits Symposium (RFIC)*. 47–50. https://doi.org/10.1109/RFIC54546.2022.9863077 ISSN: 2375-0995.

[62] Mehmet R. Yuce and Jamil Khan. 2011. *Wireless Body Area Networks: Technology, Implementation, and Applications*. CRC Press. Google-Books-ID: _NvMBQAAQBAJ.

[63] Jian-Ping Zhou, Yuan-Jun Ma, Guang-Bin Zhang, and Xiao-Ming Chen. 2014. A uniform model for direct and converse magnetoelectric effect in laminated composite. *Applied Physics Letters* 104, 20 (May 2014), 202904. https://doi.org/10.1063/1.4878559

[64] Dibin Zhu. 2009. *Methods of frequency tuning vibration based micro-generator*. phd. University of Southampton. https://eprints.soton.ac.uk/69323/